RSC Advances

PAPER

View Article Online
View Journal | View Issue

Cite this: *RSC Adv.*, 2024, **14**, 9609

Modified photoanode by *in situ* growth of covalent organic frameworks on $BiVO_4$ for oxygen evolution reaction†

Anni Guo,‡[a] Xingchun Wu,‡[a] Syed Husnain Ali,[a] Huawei Shen,[c] Ligong Chen, *[ab] Yang Li [ab] and Bowei Wang *[ab]

Received 4th February 2024
Accepted 15th March 2024

DOI: 10.1039/d4ra00899e

rsc.li/rsc-advances

The development of efficient oxygen evolution reaction (OER) catalysts is of great significance because the water oxidation reaction at the photoanode is the rate-determining step in photoelectrocatalytic (PEC) water splitting. Herein, two hybrid photoanodes named $BiVO_4$/COF-Azo and $BiVO_4$/COF-Ben were prepared by *in situ* solvothermal growth on a modified $BiVO_4$ photoanode. Characterization results revealed that the Azo and Ben COFs could match with $BiVO_4$ well to form heterojunctions, which could effectively enhance the separation efficiency of photogenerated carriers. Also, the smaller impedance of the composite photoanodes and faster kinetics of the water oxidation reaction promoted the charge transmission and enhanced the reaction efficiency of the surface-reaching holes, respectively. As a result, the composite photoanodes exhibited a larger photocurrent and more negative onset potential compared to the pristine $BiVO_4$. This work not only provides a new strategy to construct efficient hybrid photoanodes, but also expands the applications of COFs.

Introduction

With rapid industrialization and ever-increasing global population,[1] environmental pollution and the energy crisis have become the most alarming concerns globally,[2–4] which threaten the development and survival of living beings.[5] The development of renewable energy sources such as solar, ocean[6] and nuclear[7] energy is thought to be one of the effective methods to solve them. Among them, photoelectrocatalytic (PEC) decomposition of water is an important technique to convert solar energy to chemical energy,[8] which includes oxygen evolution reaction (OER) and hydrogen evolution reaction (HER).[9] However, compared with HER, OER is the rate-determining step that governs the reaction rate of the PEC water splitting, owing to the multi-electron transfer reaction pathway.[10,11] Furthermore, it is often accompanied by excessive reaction overpotential and poor reaction kinetics at the photoanode in the OER process,[12,13] so improving the performance of OER is the key to improve the photoconversion efficiency.[14] Therefore, designing and synthesizing efficient catalysts for OER is of uppermost priority.[15,16]

Covalent organic frameworks (COFs), a class of porous nanomaterials with periodically tunable structures, can be used as a functional material with promising applications in environmental regulation and energy utilization.[17,18] For example, they always combine the advantages of large specific surface area and ordered pore structure, which can provide more active sites and facilitate the mass transfer.[19] Also, their π-conjugated skeleton as 2D materials endows them with an excellent ability to harvest light and conduct electrons. More importantly, formed by the stacking of molecular layers, COFs typically have columnar π-arrays that are beneficial for electron delocalization, further promoting the separation and migration of photogenerated carriers.[20–22] Moreover, strong covalent bond linkages endow them with good chemical and thermal stabilities, which enables them to have a long lifetime. However, the fast charge recombination of most pure COFs results in their low photo- or electro-catalytic efficiency. Hence, considering that the tunable band structure of COFs can match with many inorganic semiconductors to form a built-in electric field, which is conducive to the separation of photogenerated holes and electrons, the hybridization of organic COFs and inorganic semiconductors may be a feasible strategy to boost the OER activity of photoanodes.[23]

Among inorganic semiconductors, bismuth vanadate ($BiVO_4$) is recognized as a highly promising photoanode.[24] First, its appropriate band gap (~2.4 eV) allows solar light absorption and so it has the potential as a photocatalyst driven by visible light. Second, its moderate valence band (2.4 V *vs.* the reversible hydrogen electrode, RHE) matches the thermodynamic oxygen

[a]*School of Chemical Engineering and Technology, Tianjin University, Tianjin 300350, P. R. China. E-mail: lgchen@tju.edu.cn; bwwang@tju.edu.cn*
[b]*Institute of Shaoxing, Tianjin University, Shaoxing 312300, Zhejiang, P. R. China*
[c]*Shaoxing Xingxin New Materials Co., Ltd, Shaoxing 312300, Zhejiang, P. R. China*

† Electronic supplementary information (ESI) available. See DOI: https://doi.org/10.1039/d4ra00899e

‡ These authors contributed equally to this work.

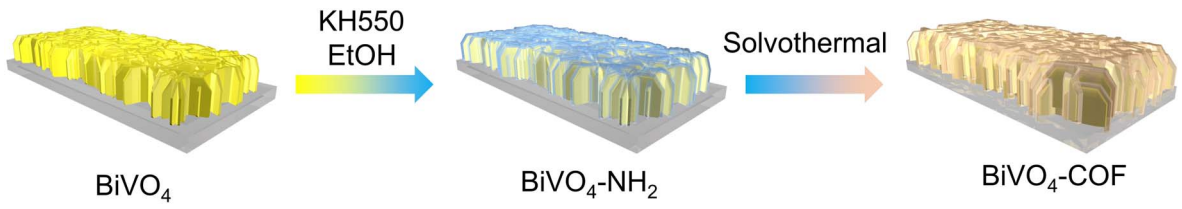

Scheme 1 Schematic illustration of the preparation of $BiVO_4$–COF photoanode.

evolution potential well. Besides, its conduction band (~0.0 V *vs.* RHE) provides a more negative photocurrent onset. Nevertheless, the application of $BiVO_4$ is still impeded on account of the low separation capacity and high electron–hole recombination rate as well as poor charge transport.[25] In this context, many modified strategies have been proposed, such as tuning the morphology, doping,[26,27] incorporating cocatalysts[28–30] and constructing heterojunctions.[31–33] Especially a heterojunction photoanode is considered as an efficient method to increase optical absorption, promote charge separation and prolong carrier lifetime. Accordingly, combining the COFs mentioned above with $BiVO_4$ to build a heterojunction photoanode may also be an effective way to enhance OER activity. However, to our best knowledge, there have been few reports on the hybridization of COFs and $BiVO_4$ as effective photoanodes for photoelectrocatalytic OER.

Herein, $BiVO_4$/COF-Azo and $BiVO_4$/COF-Ben hybrid photoanodes were successfully prepared by an *in situ* solvothermal growth method (Scheme 1). Their structures and morphology were characterized by Fourier transform infrared (FT-IR) spectroscopy, scanning electron microscopy (SEM) and transmission electron microscopy (TEM). The phase compositions and surface chemical states were studied by powder X-ray diffraction (PXRD) analysis and X-ray photoelectron spectroscopy (XPS), respectively. Due to the change of light absorption ability and energy band structures, the OER performances of two hybrid photoanodes were improved compared to that of pristine $BiVO_4$ photoanode. Furthermore, the corresponding catalytic mechanism was proposed.

Experimental section

Preparation of $BiVO_4$ seed layer[34]

The $BiVO_4$ seed layer was prepared on FTO conductive glass by the spin-coating method. Firstly, bismuth nitrate (485.1 mg) and ethylenediamine tetraacetic acid (438.4 mg) were dispersed in 15 mL ultrapure water. Then, ammonia solution (1 mL) was added to the solution to regulate pH to 10 and the mixture was stirred to be fully dissolved. The obtained solution was named solution A. Similarly, solution B was obtained by using ammonium metavanadate (117.0 mg) and ethylenediamine tetraacetic acid (146.1 mg) following the same above procedure. Mix up solution A and B evenly to yield the seed layer precursor. Secondly, the FTO conductive glass was placed on the spinner for spin-coating operation and dropped 10 drops of seed layer precursor solution, then were put in the muffle furnace at 500 °C for 3 min. Repeat the above operation for three times and take it out. Finally, the FTO conductive glass covered with $BiVO_4$ seed layer was obtained by heat treatment in the muffle furnace at 500 °C for 2 h.

Preparation of the $BiVO_4$ photoanode

The $BiVO_4$ photoanode was prepared by a seed layer-assisted hydrothermal method. Firstly, bismuth nitrate (145.5 mg) and ethylenediamine tetraacetic acid (131.5 mg) were dispersed in distilled water (30 mL). Subsequently, 2 M NaOH solution (0.75 mL) was dropped to adjust pH and the mixture was stirred to be dissolved completely. Next, ammonium metavanadate (35.1 mg) was added to the above solution with stirring. When it became yellow and transparent, pour it into a 50 mL Teflon-lined autoclave with the $BiVO_4$ seed layer substrate leaning against the autoclave wall and the seed layer side facing down. The hydrothermal process was carried out at 180 °C for 3 h to obtain the $BiVO_4$ photoanode. The reactor was cooled to room temperature and the glass was taken out with clean tweezers, washed with ultrapure water and dried in the blast drying oven. At last, the prepared photoanode was calcined at 500 °C for 4 h.

Synthesis of the $BiVO_4$/COF-Azo photoanode

The $BiVO_4$/COF-Azo was prepared by *in situ* solvothermal growth method. Firstly, 0.2 mL γ-aminopropyltriethoxysilane was dissolved in 10 mL absolute ethanol and the prepared $BiVO_4$ photoanode was immersed in it for 12 h, then taken out and dried to complete the amination modification process. Secondly, the aminated $BiVO_4$ photoanode was placed into 5 mL *N*,*N*-dimethylacetamide (DMAc) solution dissolving 5 mg 1,3,5-triformylphloroglucinol at room temperature for 1 h. Then, 1,3,5-triformylphloroglucinol (21 mg, 0.1 mmol), 4,4′-azodianiline (32 mg, 0.15 mmol) and *N*,*N*-dimethylacetamide/*o*-dichlorobenzene (2 mL, 1/1 v/v) were added to a 10 mL Pyrex tube. The reactants were dispersed by ultrasonication for 10 min and then the above treated $BiVO_4$ photoanode was put into the mixture. After being degassed through three freeze–pump–thaw cycles, the tubes were vacuum sealed and placed in an oven for 4 days at 120 °C. Finally, when cooled to room temperature after the reaction, the photoanode was taken out and the powders in the tube were filtered out. Then both were dried under vacuum at 80 °C for 12 h after being washed thoroughly with DMF, acetone and methanol.

Synthesis of the $BiVO_4$/COF-Ben photoanode

The prepared $BiVO_4$ photoanode was immersed into 5 mL DMAc solution dissolving 5 mg 1,3,5-triformylphloroglucinol at

room temperature for 1 h. 1,3,5-Triformylphloroglucinol (21 mg, 0.1 mmol), 4,4′-diamino-*p*-terphenyl (39 mg, 0.15 mmol) and dioxane/mesitylene (3 mL, 2/1 v/v) were added to a 10 mL Pyrex tube. The reactants were dispersed by ultrasonication for 10 min and then the above treated $BiVO_4$ photoanode was put into the mixture. After being degassed through three freeze–pump–thaw cycles, the tubes were vacuum sealed and placed in an oven for 3 days at 150 °C. Finally, when cooled to room temperature after the reaction, the photoanode was taken out and the powders in the tube were filtered out. Then both were dried under vacuum at 80 °C for 12 h after being washed thoroughly with DMF, acetone and methanol.

Results and discussion

Characterization of photoanodes

The morphologies of $BiVO_4$ photoanode before and after modified by COF were examined by SEM and TEM. As can be seen from the SEM images (Fig. 1), pure $BiVO_4$ photoanode was composed of nanoplate arrays with a thickness of approximately 250 nm, forming a thin film with a thickness of 1.4 μm on the FTO conductive glass. Their close contact was conducive to the rapid separation of photogenerated electrons and holes. After *in situ* growth of COF-Azo and COF-Ben, the pristine $BiVO_4$ nanoplate morphology was maintained, but the aggregated particles uniformly covered the surface of nanoplate structure to make it rougher, indicating the successful integration of the COF layer. From the high-resolution TEM images (Fig. S1†), it exhibited obvious lattice fringes on the $BiVO_4$ layer, indicating its high crystallinity with few intrinsic defects. The EDS mapping images showed that V, Bi, C, N and O were all uniformly distributed in $BiVO_4$/COF-Azo and $BiVO_4$/COF-Ben. However, the distribution ranges of N and C elements were a little bit larger than the other three elements, further demonstrating the uniform and complete coating by two COFs on the surface of $BiVO_4$ nanoplates. Their close contact can effectively extract photo-induced holes from the semiconductor and promote the water oxidation reaction.

Subsequently, the phase composition of the prepared photoanode was characterized by powder X-ray diffraction. There was a negligible difference between the XRD patterns of the two composite photoanodes and pure $BiVO_4$ photoanode (Fig. S2†). They all displayed the diffraction peaks of FTO conductive glass and monoclinic scheelite of $BiVO_4$, indicating that the composite of COF had no effect on the phase composition of the $BiVO_4$ photoanode. However, compared with the standard PDF card (JCPDS No. 44-0081), there was no diffraction peak with 2θ of 30.5° in the XRD pattern of $BiVO_4$, which corresponded to the (0 4 0) crystal plane. It implied that the growth of $BiVO_4$ crystal in this direction was inhibited, which might also be the reason why $BiVO_4$ crystal finally grew into nanosheets. In order to confirm the formation of crystalline COFs, the powders in Pyrex tube were collected by filtration and characterized by XRD (Fig. S3†). It was found that there was a main diffraction peak at 3.12° for COF-Azo and 2.72° for COF-Ben, respectively. In addition, the experimental PXRD patterns of the COFs were both highly consistent with the simulated stacking model. COFs with high crystallinity can improve the efficiency of mass transfer and make holes transfer to the surface of the photoanode quickly to participate in the OER. Furthermore, the structures of COF-Azo, COF-Ben and their corresponding composites with $BiVO_4$ were confirmed by FT-IR spectroscopy (Fig. S4a†). It was shown that two new vibration peaks at 1618 cm^{-1} and 1577 cm^{-1} were observed in the spectra of COF-Azo and COF-Ben, which were attributed to C=O and C=C in the β-ketoamine linkages. Their appearance proved that both

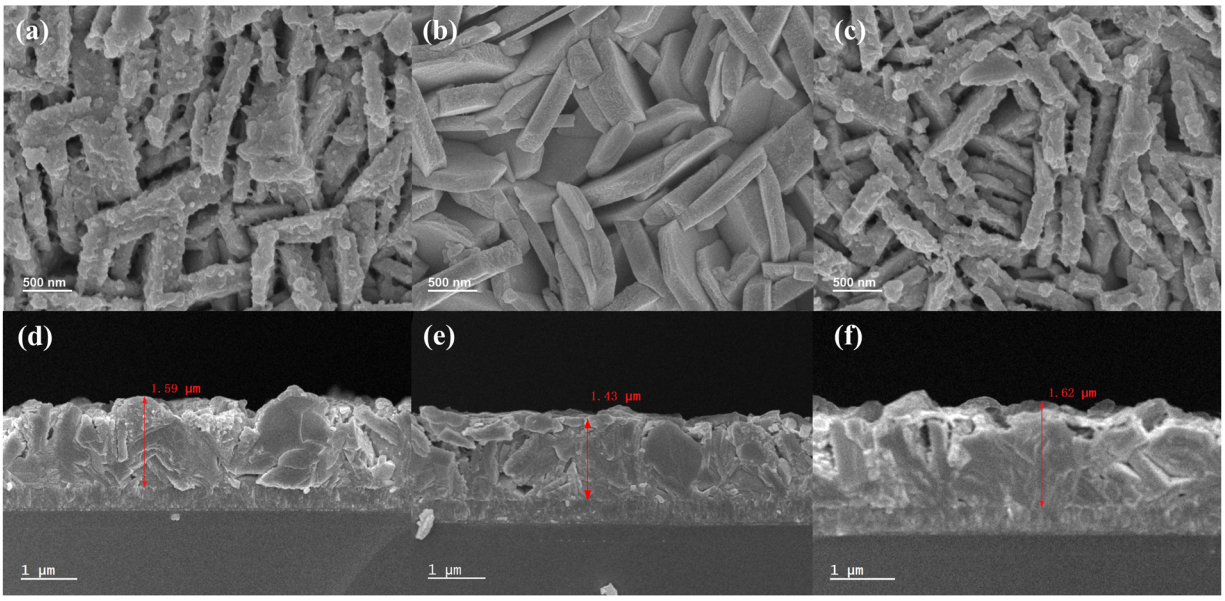

Fig. 1 Zenithal SEM images of (a) $BiVO_4$/COF-Azo, (b) $BiVO_4$, (c) $BiVO_4$/COF-Ben and cross-sectional SEM images of (d) $BiVO_4$/COF-Azo, (e) $BiVO_4$, (f) $BiVO_4$/COF-Ben.

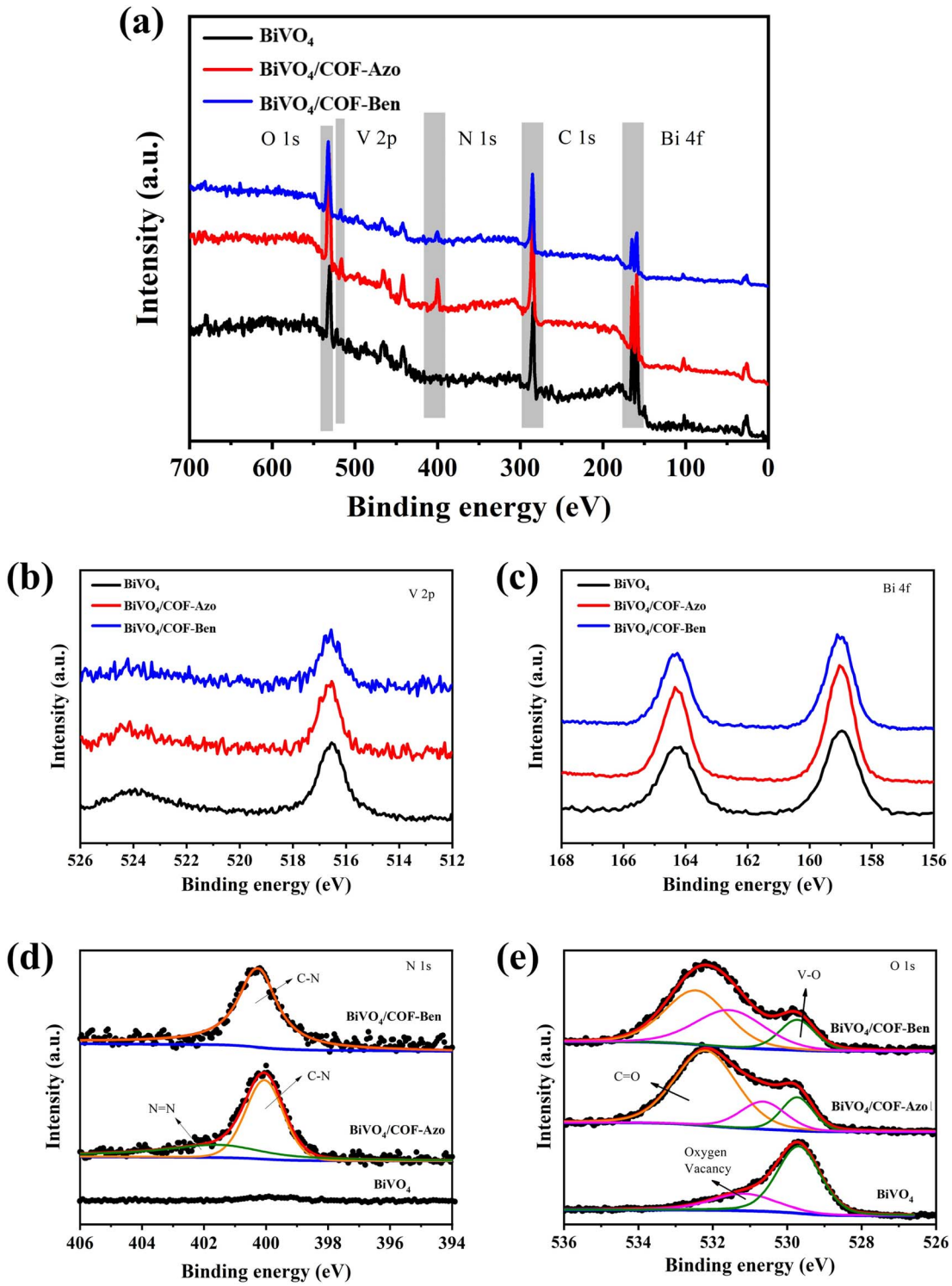

Fig. 2 The full survey spectra, (b) V 2p, (c) Bi 4f, (d) N 1s and (e) O 1s high-resolution XPS spectra of $BiVO_4$, $BiVO_4$/COF-Azo and $BiVO_4$/COF-Ben photoanodes.

COF-Azo and COF-Ben were synthesized successfully. Compared with the spectrum of TP, the peaks at 1643 cm^{-1} and 2897 cm^{-1} corresponding to C=O and C–H stretching of formyl totally disappeared in the spectra of COF-Azo and COF-Ben. Similarly, the N–H stretching bands (at 3300–3500 cm^{-1}) presented in Azo and Ben also appeared to weaken obviously in the spectra of them. These results indicated the effective condensation between aldehyde groups of TP and amino groups of Azo and Ben. In addition, from Fig. S4b,† it was found that $BiVO_4$/COF-Azo and $BiVO_4$/COF-Ben obtained by *in situ*

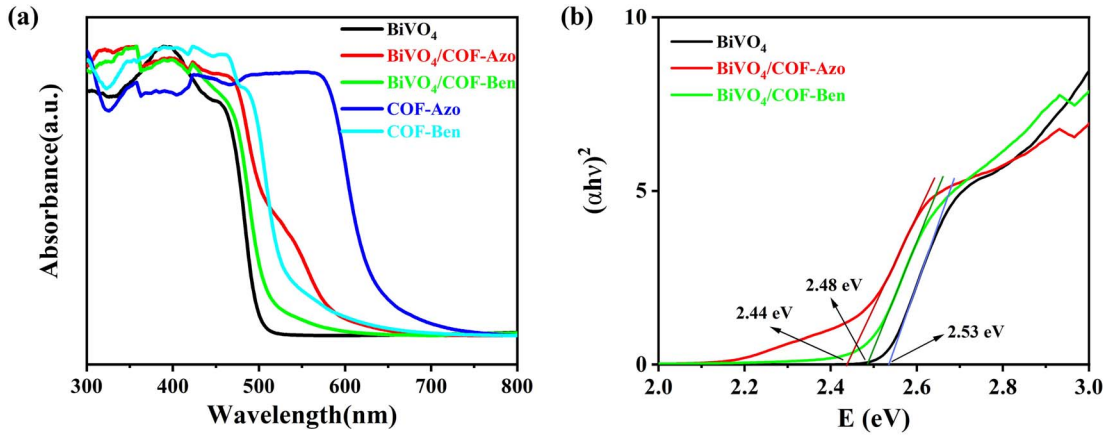

Fig. 3 (a) UV-vis diffuse reflectance spectra of $BiVO_4$, COF-Azo, COF-Ben, $BiVO_4$/COF-Azo and $BiVO_4$/COF-Ben photoanodes; (b) Tauc curves of $BiVO_4$, $BiVO_4$/COF-Azo and $BiVO_4$/COF-Ben photoanodes.

growth not only retained the characteristic peaks of COF-Azo and COF-Ben, but also displayed a wide peak at 700 cm^{-1} similar to that of $BiVO_4$, which demonstrated the exact hybridization of COF and $BiVO_4$. The surface chemical states before and after combining were measured by XPS. According to the full-spectra scan of $BiVO_4$, $BiVO_4$/COF-Azo and $BiVO_4$/COF-Ben, they all exhibited C, O, V and Bi elements, while N 1s peak only appeared in two composites (Fig. 2a). These results were consistent with EDS mapping. It is worth noting that there was a peak corresponding to N=N in addition to C–N in the N 1s spectrum of $BiVO_4$/COF-Azo (Fig. 2d). Moreover, a C=O peak appeared after combination from the high-resolution XPS spectrum of O 1s (Fig. 2e). Combined with the FT-IR spectrum, it was assigned to the C=O functional group in COFs, while the peak at 399.96 eV in the N 1s spectrum corresponded to –C–N– bond from COFs or the connection bonds between COFs and aminated $BiVO_4$ (Fig. 2d). The above phenomena further proved the successful synthesis of COFs and effective coating on $BiVO_4$ surface.

For photoelectrocatalysis, one of the important factors is the light absorption ability of photoelectric materials. Therefore, the UV-vis diffuse reflectance spectra of $BiVO_4$/COF-Azo and $BiVO_4$/COF-Ben before and after combining were collected (Fig. 3a). It was shown that the absorption wavelength ranges of COF-Azo and COF-Ben were both larger than that of pure $BiVO_4$. Specifically, the absorption range of COF-Azo was 300–700 nm, revealing the strongest absorption ability among them. The maximum absorption edge of pristine $BiVO_4$ photoanode was about 510 nm, while those of $BiVO_4$/COF-Azo and $BiVO_4$/COF-Ben became 650 nm and 600 nm, respectively. Additionally, a shoulder peak was observed in the spectrum of $BiVO_4$/COF-Azo. These changes would greatly improve their absorption ability, thereby enhancing the utilization rate of visible light in a larger wavelength range. Transforming the above spectra by the Tauc plot method, the band gaps of three photoanodes were obtained. As shown in Fig. 3b, the band gap of $BiVO_4$ is 2.53 eV, while that of $BiVO_4$/COF-Azo and $BiVO_4$/COF-Ben is 2.44 eV and 2.48 eV, respectively. The change of band gap indicated that

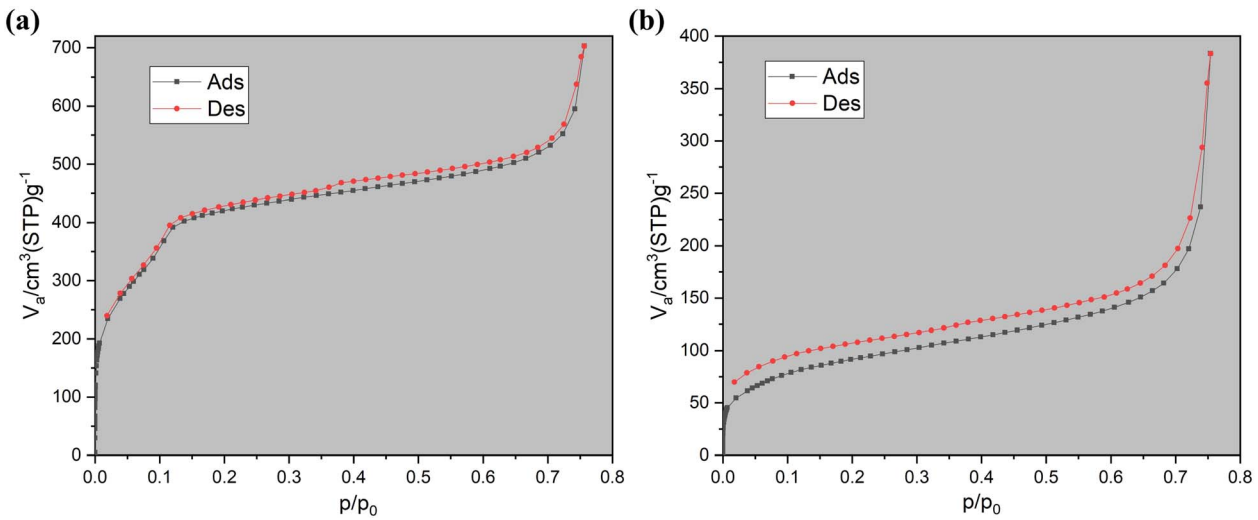

Fig. 4 N_2 adsorption/desorption isotherms for COF-Azo (a) and COF-Ben (b).

there was interaction between $BiVO_4$ and COFs, which would be beneficial to the conduction of photogenerated carriers so as to increase their photoelectrocatalytic performance. To explore the influence of the specific surface areas on the performance of the photoanode, the specific surface areas of COF-Azo and COF-Ben powders collected from the tube were calculated by nitrogen sorption isotherms at 77 K (Fig. 4). The Brunauer–Emmett–Teller (BET) specific surface areas of COF-Azo powders was calculated to be 151.48 $m^2\ g^{-1}$, while that of COF-Ben is 61.61 $m^2\ g^{-1}$. The larger BET specific surface area will be more conducive to mass transfer and increase the contact area between photoanode and electrolyte, thereby accelerating the progress of OER.

Photoelectrochemical performance

The contribution of COF to the photoelectrochemical performance in a water splitting setup was investigated by a series of photoelectrochemical tests. Firstly, the linear sweep voltammetry (LSV) curves that can reflect the water oxidation activity directly were obtained. As shown in Fig. 5a, the pristine $BiVO_4$ exhibited an obvious photocurrent density of 0.82 mA cm^{-2} at 1.23 V (*vs.* RHE) and an onset potential of 0.7 V (*vs.* RHE), indicating that the $BiVO_4$ photoanode could absorb and convert solar energy to catalyze the OER effectively under illumination. It was assumed that the high photocurrent density was attributed to the ordered crystal structure and orientation, which were conducive to the transfer and separation of photogenerated carriers.[35] Compared to the pristine $BiVO_4$, both $BiVO_4$/COF-Azo and $BiVO_4$/COF-Ben composite photoanodes showed a higher photocurrent at all potentials. Specifically, the photocurrent density of $BiVO_4$/COF-Azo increased from 0.82 mA cm^{-2} to 1.38 mA cm^{-2} at 1.23 V (*vs.* RHE), while that of $BiVO_4$/COF-Ben only increased to 1.08 mA cm^{-2} at the same voltage, although their onset potential both negatively shifted to 0.6 V (*vs.* RHE). The enhanced PEC performance of composite photoanodes demonstrated that the COF species played a positive role in the photoelectrocatalytic water oxidation reaction. Furthermore, the photocurrent transients of the photoanodes were also measured to reflect their photoelectric response performance. The *I–t* curves showed that the hybrid photoanodes displayed a higher photocurrent density than that of the pristine photoanode, which implied that modifying $BiVO_4$ with COF can improve the photoanode performance effectively (Fig. 5b). To be specific, the photocurrent density of $BiVO_4$/COF-Azo and $BiVO_4$/COF-Ben photoanodes was increased to 1.5 and 1.25 times of $BiVO_4$, respectively, which was consistent with LSV curves. Then, the stability of $BiVO_4$/COF-Azo photoanode with the best performance was evaluated (Fig. S5†). It was found that $BiVO_4$/COF-Azo photoanode exhibited good stability and 80% of the initial catalytic performance could still be maintained after 5 h, which might be related to the high stability of COF-Azo.

In addition, a series of measurements were conducted to explore the exact mechanism. Generally, sulfite oxidation reaction has faster kinetics than OER, so the surface-reaching holes can quickly participate in the oxidation reaction with nearly 100% efficiency. Based on this fact, the ratio of the water oxidation current to sulfite oxidation current can be used to reflect the reaction efficiency of surface-reaching holes.[36] As shown in Fig. 6a, it was clear that the $BiVO_4$/COF-Azo and $BiVO_4$/COF-Ben hybrid photoanodes exhibited a higher oxidation current than the pristine one in the presence of Na_2SO_3, which was speculated that COF could promote the conduction of photogenerated holes to the surface of photoanodes to participate in OER. Compared to $BiVO_4$/COF-Ben, the oxidation current of $BiVO_4$/COF-Azo was higher, indicatingCOF-Azo can accelerate the above conduction process. By calculating the $J_{water}/J_{surface}$ ratio that was considered as the yield of holes that participate in the water oxidation reaction at the electrolyte/semiconductor interface ($\eta_{surface}$), the reaction efficiency of the surface-reaching holes was obtained. From Fig. 6b, the composite photoanodes $BiVO_4$/COF-Azo and $BiVO_4$/COF-Ben both showed a much higher reaction efficiency than that of pristine $BiVO_4$ photoanode. It indicated that the surface-reaching holes tended to react with water more quickly and

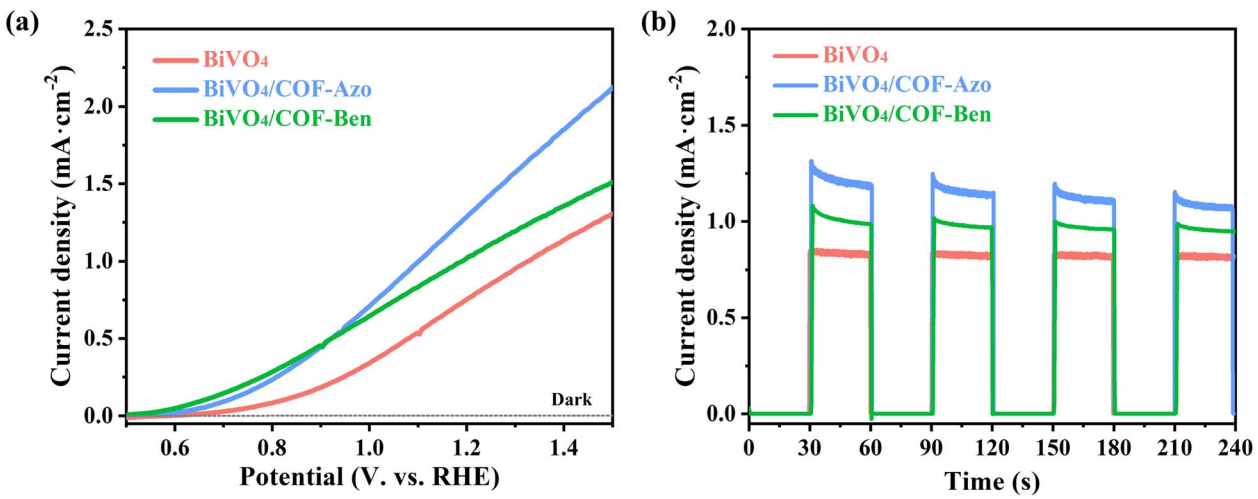

Fig. 5 (a) LSV curves and OER curves without illumination; (b) *I–t* curves of $BiVO_4$, $BiVO_4$/COF-Azo and $BiVO_4$/COF-Ben photoanodes.

efficiently after the modification with COFs, which further confirmed that the integrated COFs can improve interface properties and boost the water oxidation reaction. The electrochemical impedance spectra (EIS) were also recorded to figure out the transfer of carriers in the PEC system. As presented in Fig. 6c, three curves all exhibited a typical resistance arc, but the smaller radius for the modified photoanode was compared with that for the pure $BiVO_4$ photoanode, which meant that the former possessed a better ability to transfer the carrier. Among them, the resistance arc radius of $BiVO_4$/COF-Azo was the smallest, revealing its minimal charge transfer impedance in the reaction and the best ability to transfer carriers. Thus, it was easiest for $BiVO_4$/COF-Azo to transfer photogenerated holes to the surface of the photoanode, thereby showing the most outstanding OER performance. Considering that the intrinsic properties of the photoanode were unlikely to be changed just by the modification of COFs, the OER curves of two $BiVO_4$/COF and original $BiVO_4$ photoanodes in the absence of illumination were recorded as well, which verified the change of electrocatalytic OER performance after combining COFs (Fig. 6d). It was found that the photocurrent density of $BiVO_4$/COF-Azo and $BiVO_4$/COF-Ben photoanodes was much higher than that of the pristine $BiVO_4$ when voltage was more than 2.0 V (*vs.* RHE) without illumination. Higher photocurrent density and lower overpotential meant better electrocatalytic performance. Therefore, the two composite photoanodes had higher water oxidation activity and more negative initial potential of oxygen evolution, which made their water oxidation reaction kinetics faster and could make use of the holes reaching the surface of the photoanodes more effectively. At the same time, the curves of $BiVO_4$/COF-Azo and $BiVO_4$/COF-Ben basically coincided, proving that the main difference of their photoelectrocatalytic OER performance came from the influence of light rather than electricity.

Finally, the interaction between $BiVO_4$ and COF was further explored by testing the band structure of photoanodes before and after combination (Fig. 7). It can be inferred from Tauc and M–S diagrams that both COF-Azo and COF-Ben belong to N-type semiconductors with band gaps of 2.02 eV and 2.39 eV, respectively. Concretely, the conduction band position of COF-Azo is about 0.22 V (*vs.* RHE), so the valence band position is about 2.24 V (*vs.* RHE); the conduction band position of COF-

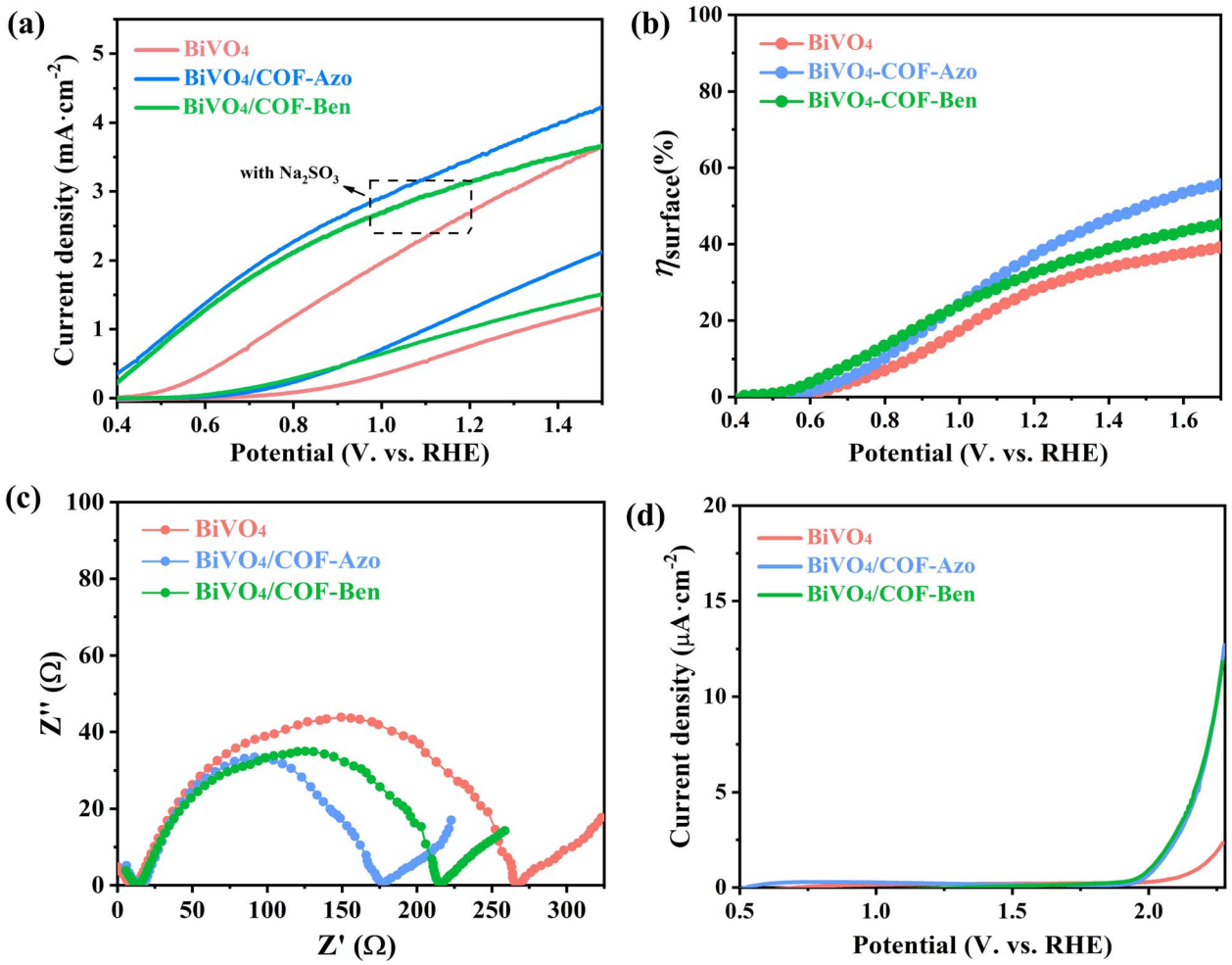

Fig. 6 (a) Sulfite and water oxidation current curves; (b) surface hole reaction efficiency; (c) EIS curves; (d) LSV curves and OER curves without illumination of $BiVO_4$, $BiVO_4$/COF-Azo and $BiVO_4$/COF-Ben photoanodes.

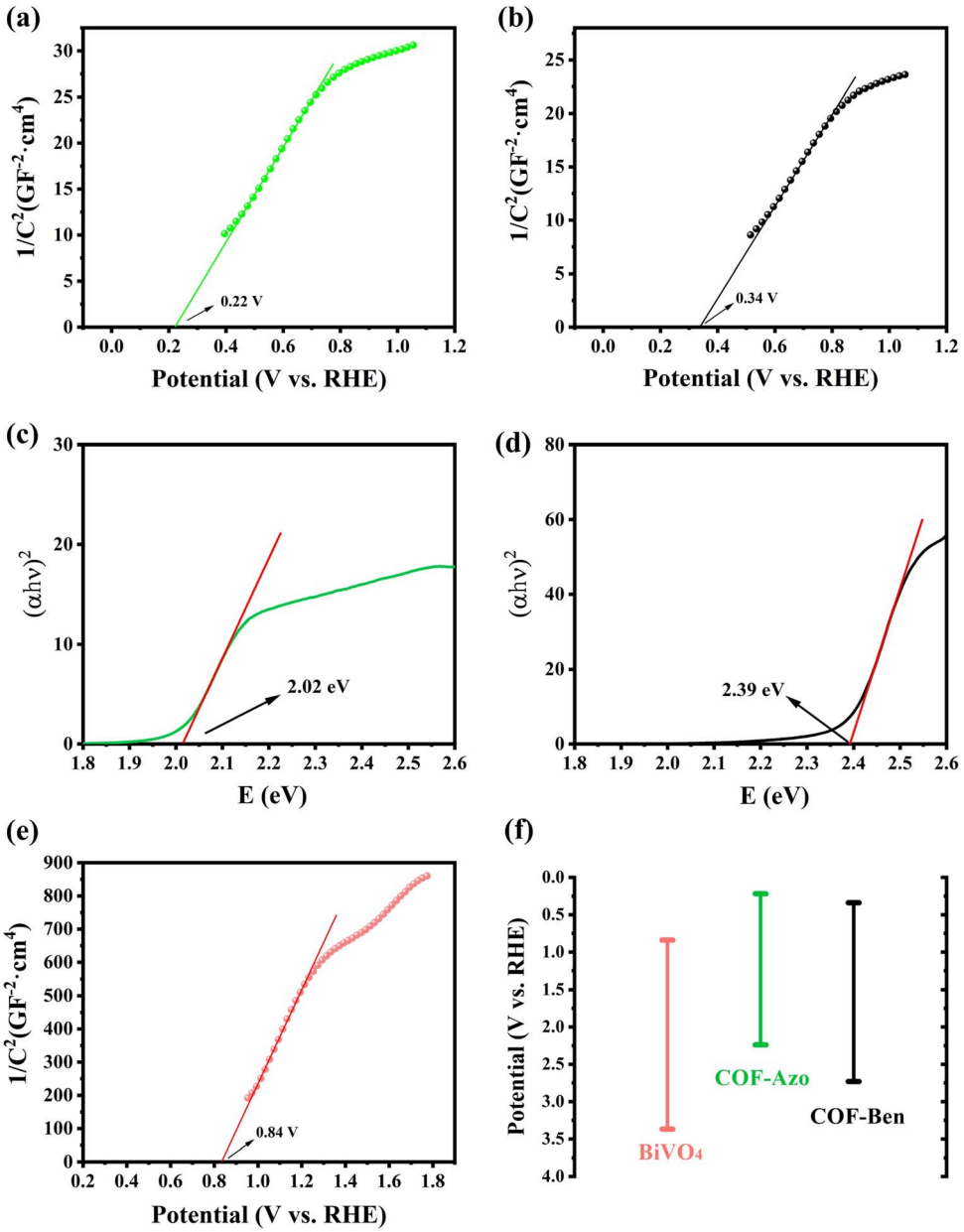

Fig. 7 (a) M–S curve of COF-Azo; (b) M–S curve of COF-Ben; (c) Tauc curve of COF-Azo; (d) Tauc curve of COF-Ben; (e) M–S curve of $BiVO_4$; (f) band structure diagram of $BiVO_4$, COF-Azo and COF-Ben.

Ben is about 0.34 V (*vs.* RHE), so the valence band position is about 2.73 V (*vs.* RHE); the conduction band position of $BiVO_4$ is about 0.84 V (*vs.* RHE) and the forbidden bandwidth is 2.53 eV, so the valence band position is about 3.37 V (*vs.* RHE). According to the above values, the energy band structure diagram was shown in Fig. 7f. It can be seen that the conduction band and valence band of COF-Azo and COF-Ben were higher than those of $BiVO_4$. Therefore, heterojunction can be formed by combination so that the separation efficiency of photogenerated carriers was enhanced and the recombination rate was reduced. As a result, electrons gathered at $BiVO_4$, while holes moved to COFs. It made more photogenerated holes reach the surface of photoanodes to participate in the reaction, which further improved the photoelectrocatalytic OER performance.

Conclusion

In summary, two composite photoanodes, $BiVO_4$/COF-Azo and $BiVO_4$/COF-Ben, have been synthesized by *in situ* growth of COF on $BiVO_4$ *via* covalent bonding. Comprehensive characterization results including SEM, TEM, FT-IR, XPS and EDS mapping confirmed the successful hybridization of $BiVO_4$ with COF-Azo and COF-Ben, respectively. The experimental results showed that the catalytic performances of two hybrid photoanodes were significantly improved compared with pristine $BiVO_4$. Particularly, the photoelectrocatalytic property of $BiVO_4$/COF-Azo was superior to that of $BiVO_4$/COF-Ben, which might be attributed to its better light absorption ability. Moreover, the mechanism was proposed according to various electrochemical and

spectroscopic tests. The suitable energy band structure of COFs could match with $BiVO_4$ well to form heterojunction, which can improve the separation efficiency of photogenerated carriers and inhibit the recombination. In addition, the smaller impedance of the composite photoanodes and faster kinetics of water oxidation reaction kinetics both contributed to the enhancement of OER performance. Thus, this study not only provides a feasible way to design efficient photoanode, but also expands the potential applications of COFs.

Author contributions

Anni Guo: conceptualization, investigation, formal analysis, validation, writing – original draft, writing – review & editing. Xingchun Wu: conceptualization, investigation, formal analysis, validation, writing – original draft. Syed Husnain Alia: writing – review & editing. Huawei Shen: writing – review & editing. Bowei Wang: supervision, project administration, writing – review & editing. Yang Li: supervision, project administration. Ligong Chen: supervision, project administration.

Conflicts of interest

The authors declare no competing financial interest.

Acknowledgements

This work was supported by the Natural Science Foundation of Tianjin (Grant No. 22JCQNJC00230). The authors thank Ying Ha from Analysis and Testing Center of School of Environmental Science and Engineering, Tianjin University for the assistance in measurement.

References

1 S. Mukherjee, S. Dutta, Y. D. More, S. Fajal and S. K. Ghosh, *Dalton Trans.*, 2021, **50**, 17832–17850.
2 D.-G. Wang, T. Qiu, W. Guo, Z. Liang, H. Tabassum, D. Xia and R. Zou, *Energy Environ. Sci.*, 2021, **14**, 688–728.
3 R. Fouquet, *Nat. Energy*, 2016, **1**, 16098.
4 K. He, G. Chen, G. Zeng, A. Chen, Z. Huang, J. Shi, T. Huang, M. Peng and L. Hu, *Appl. Catal., B*, 2018, **228**, 19–28.
5 S. Dutta, S. Let, S. Sharma, D. Mahato and S. K. Ghosh, *Chem. Rec.*, 2021, **21**, 1666–1680.
6 S. Dutta, R. F. de Luis, J. Goscianska, A. Demessence, R. Ettlinger and S. Wuttke, *Adv. Funct. Mater.*, 2023, 2304790.
7 Y. D. More, S. Mollick, S. Saurabh, S. Fajal, M. Tricarico, S. Dutta, M. M. Shirolkar, W. Mandal, J. C. Tan and S. K. Ghosh, *Small*, 2024, **20**, e2302014.
8 T. Sick, A. G. Hufnagel, J. Kampmann, I. Kondofersky, M. Calik, J. M. Rotter, A. Evans, M. Döblinger, S. Herbert, K. Peters, D. Böhm, P. Knochel, D. D. Medina, D. Fattakhova-Rohlfing and T. Bein, *J. Am. Chem. Soc.*, 2018, **140**, 2085–2092.
9 A. Landman, H. Dotan, G. E. Shter, M. Wullenkord, A. Houaijia, A. Maljusch, G. S. Grader and A. Rothschild, *Nat. Mater.*, 2017, **16**, 646–651.
10 N. T. Suen, S. F. Hung, Q. Quan, N. Zhang, Y. J. Xu and H. M. Chen, *Chem. Soc. Rev.*, 2017, **46**, 337–365.
11 Y. Li, F.-M. Li, X.-Y. Meng, S.-N. Li, J.-H. Zeng and Y. Chen, *ACS Catal.*, 2018, **8**, 1913–1920.
12 G. Wu, K. L. More, C. M. Johnston and P. Zelenay, *Science*, 2011, **332**, 443–447.
13 K. Zhu, X. Zhu and W. Yang, *Angew. Chem., Int. Ed.*, 2019, **58**, 1252–1265.
14 Y. Yu, Z. Zhang, X. Yin, A. Kvit, Q. Liao, Z. Kang, X. Yan, Y. Zhang and X. Wang, *Nat. Energy*, 2017, **2**, 17045.
15 Q. Hu, G. Li, X. Liu, B. Zhu, X. Chai, Q. Zhang, J. Liu and C. He, *Angew. Chem., Int. Ed.*, 2019, **58**, 4318–4322.
16 J. Zhang, J. Liu, L. Xi, Y. Yu, N. Chen, S. Sun, W. Wang, K. M. Lange and B. Zhang, *J. Am. Chem. Soc.*, 2018, **140**, 3876–3879.
17 S. Fajal, S. Dutta and S. K. Ghosh, *Mater. Horiz.*, 2023, **10**, 4083–4138.
18 F. Ahmadijokani, A. Ghaffarkhah, H. Molavi, S. Dutta, Y. Lu, S. Wuttke, M. Kamkar, O. J. Rojas and M. Arjmand, *Adv. Funct. Mater.*, 2023, 2305527.
19 H. Xu and D. Jiang, *Nat. Chem.*, 2014, **6**, 564–566.
20 S. Jin, M. Supur, M. Addicoat, K. Furukawa, L. Chen, T. Nakamura, S. Fukuzumi, S. Irle and D. Jiang, *J. Am. Chem. Soc.*, 2015, **137**, 7817–7827.
21 C. Wang, Z. Zhang, Y. Zhu, C. Yang, J. Wu and W. Hu, *Adv. Mater.*, 2022, **34**, e2102290.
22 Y. Zhong, W. Dong, S. Ren and L. Li, *Adv. Mater.*, 2024, **36**, e2308251.
23 M. Zhang, M. Lu, Z.-L. Lang, J. Liu, M. Liu, J.-N. Chang, L.-Y. Li, L.-J. Shang, M. Wang, S.-L. Li and Y.-Q. Lan, *Angew. Chem., Int. Ed.*, 2020, **59**, 6500–6506.
24 S. Wang, P. Chen, Y. Bai, J.-H. Yun, G. Liu and L. Wang, *Adv. Mater.*, 2018, **30**, 1800486.
25 X. T. Gao, Z. Q. Bai, S. Zhang, J. C. Liu and Z. H. Li, *RSC Adv.*, 2020, **10**, 45067–45075.
26 S. Saxena, A. Verma, K. Asha, N. K. Biswas, A. Banerjee, V. R. Satsangi, R. Shrivastav and S. Dass, *Int. J. Hydrogen Energy*, 2020, **45**, 26746–26757.
27 H. S. Park, K. E. Kweon, H. Ye, E. Paek, G. S. Hwang and A. J. Bard, *J. Phys. Chem. C*, 2011, **115**, 17870–17879.
28 R. L. Hu, L. X. Meng, J. X. Zhang, X. Wang, S. J. Wu, Z. Wu, R. Zhou, L. Li, D. S. Li and T. Wu, *Nanoscale*, 2020, **12**, 8875–8882.
29 L. J. Wu, L. Wang, J. Zhu, M. Sun, X. H. Liu, P. Schmuki and J. Zhang, *J. Mater. Chem. A*, 2020, **8**, 2563–2570.
30 G. Z. Fang, Z. F. Liu, C. C. Han, P. Wang, X. G. Ma, H. Lv, C. Y. Huang, Z. W. Cheng and Z. F. Tong, *ACS Appl. Energy Mater.*, 2021, **4**, 3842–3850.
31 S. Bai, J. Han, Y. Zhao, H. Chu, S. Wei, J. Sun, L. Sun, R. Luo, D. Li and A. Chen, *Renewable Energy*, 2020, **148**, 380–387.
32 F. Chen, Q. Yang, J. Sun, F. Yao, S. Wang, Y. Wang, X. Wang, X. Li, C. Niu, D. Wang and G. Zeng, *ACS Appl. Mater. Interfaces*, 2016, **8**, 32887–32900.

33 B. Zhang, S.-Y. Zhao, H.-H. Wang, T.-J. Zhao, Y.-X. Liu, L.-B. Lv, X. Wei, X.-H. Li and J.-S. Chen, *Chem. Commun.*, 2017, **53**, 10544–10547.
34 B. Gao, T. Wang, X. Fan, H. Gong, X. Meng, P. Li, Y. Feng, X. Huang, J. He and J. Ye, *Sol. RRL*, 2018, **2**, 1800102.
35 C. W. Kim, Y. S. Son, M. J. Kang, D. Y. Kim and Y. S. Kang, *Adv. Energy Mater.*, 2016, **6**, 1501754.
36 T. W. Kim and K.-S. Choi, *Science*, 2014, **343**, 990–994.